



Contents lists available at ScienceDirect

Chemical Engineering Research and Design

journal homepage: www.elsevier.com/locate/cherdiChemE
ADVANCING
CHEMICAL
ENGINEERING
WORLDWIDE

Mass transfer from a soluble Taylor bubble to the surrounding flowing liquid in a vertical macro tube — A numerical approach

M.C.F. Silva, J.B.L.M. Campos, J.D.P. Araújo*

Centro de Estudos de Fenómenos de Transporte, Departamento de Engenharia Química, Faculdade de Engenharia da Universidade do Porto, Rua Dr. Roberto Frias, 4200-465, Porto, Portugal

ARTICLE INFO

Article history:

Received 23 October 2018

Received in revised form 22 January 2019

Accepted 25 January 2019

Available online 1 February 2019

Keywords:

Mass transfer

Slug flow

CFD

VOF

Oxygen

ABSTRACT

Gas–liquid mass transfer is a phenomenon with a wide practical relevance and, besides many other possible advantages, its fundamentals can be used to enhance or regulate chemical and biological processes. In this work, the specific case of the mass transfer of oxygen from a Taylor bubble to the surrounding flowing liquid was studied using CFD techniques. This study was performed for a range of flow conditions (different Reynolds numbers) and a liquid with a viscosity (and constant Morton number) typical of bio-fluids. The flow field, gas–liquid interface and concentration field were determined simultaneously by coupling the VOF methodology with the species mass balance equation and setting a constant solute concentration at the bubble surface. The mass transfer behavior on the different hydrodynamic regions (nose, film and tail) was inspected and quantified based on local coefficients. It was possible to verify that these values increase along the nose and reach a maximum at the fully developed film region, where it tends to stabilize regardless of the bubble length (for bubble lengths between 2D and 9D). An opposite tendency was found along the bubble tail, where a decrease was verified on the local mass transfer coefficient values. Average mass transfer coefficients based on the simulation data were also determined. The comparison of these results with theoretical predictions allowed to infer that the film theory is the most adequate to describe the gas–liquid mass transfer between a Taylor bubble and the surrounding liquid.

© 2019 Institution of Chemical Engineers. Published by Elsevier B.V. All rights reserved.

1. Introduction

In several industrial equipment, the presence of either micro and macroorganisms in excess leads to a problem known as biofouling (Bott, 1995). Although in more specific cases (such as seawater-cooled equipment) macroorganisms may create operational difficulties, the main concern in most of the equipment is the presence of bacteria and biofilm formation over the dispositive walls.

It is known that in thermal equipment, the adhesion of any type of fouling, and consequently of biofilms, creates an additional thermal resistance which reduces the thermal efficiency. In addition, biofilms can also raise problems of public health (Characklis, 1981). One exam-

ple, is the presence of biofilms on dairy manufacturing plants. Once the biofilm is established, it can act as a source of contamination to products and/or other surfaces. The growth of biofilms on pasteurizers contaminates the milk and reduces its quality and of other derivative products (Flint et al., 1997).

While the presence of biofilms in thermal equipment is undesirable, the same cannot be generalized for other equipment. Biofilm reactors are used to obtain several products (Cheng et al., 2010) like organic acids (Sanromán et al., 1996), ethanol (Demirci et al., 1997) and antibiotics (Park et al., 1989), among others. Besides, the water industry also relies on the presence of microorganisms to help control the quality of water (Kumar and Lin, 2010; Qureshi et al., 2001). Depending on the type

* Corresponding author.

E-mail address: daraujo@fe.up.pt (J.D.P. Araújo).<https://doi.org/10.1016/j.cherd.2019.01.022>

0263-8762/© 2019 Institution of Chemical Engineers. Published by Elsevier B.V. All rights reserved.

Nomenclature

A	Interfacial area m^2
c	Concentration kg m^{-3}
c^*	Saturation concentration kg m^{-3}
$C_{A,i}$	Concentration at the interface mol m^{-3}
C_{bulk}	Concentration in the bulk mol m^{-3}
c_{dis}	Concentration on the cell center kg m^{-3}
D	Tube diameter m
D_L	Coefficient of diffusion $\text{m}^2 \text{s}^{-1}$
\vec{F}	External body force N m^{-3}
g	Gravitational acceleration $\text{m}^2 \text{s}^{-1}$
h	Distance along the normal to the gas interface m
$I(l/D)$	Function of the bubble shape
\bar{J}_i	Diffusive flux of specie i $\text{kg m}^{-2} \text{s}^{-1}$
k_L	Mass transfer coefficient for the liquid phase m s^{-1}
\bar{k}_L	Average/global mass transfer coefficient for the liquid phase m s^{-1}
k_{LA}	Volumetric liquid side mass transfer coefficient $\text{m}^3 \text{s}^{-1}$
l	Distance from the nose tip to the liquid film fully developed m
L_s	Taylor bubble length m
\vec{n}	Normal vector
N_A	Mass transfer rate kg s^{-1}
p	Static pressure Pa
P_c	Cell center position
P_i	Initial position
P_n	Computed position
r	Radial coordinate m
s	Coordinate along the bubble surface m
s_t	Bubble perimeter m
t	Time s
t_c	Gas–liquid contact time s
u	Velocity at the bubble interface m s^{-1}
\vec{u}	Velocity vector m s^{-1}
\bar{U}_L	Average liquid velocity m s^{-1}
\bar{U}_L^{MFR}	Average liquid velocity expressed in a moving reference frame m s^{-1}
\bar{U}_F^F	Average film velocity m s^{-1}
U_∞	Bubble rising velocity through stagnant liquid m s^{-1}
U_B	Bubble rising velocity m s^{-1}
y_i	Local mass fraction of specie i
z	Axial coordinate m
z_o	Axial coordinate at the nose tip m
z_t	Axial coordinate at the tail tip m

Greek letters

α	Volume fraction
δ_c	Thickness of the concentration boundary layer m
δ_h	Film thickness m
μ	Viscosity Pa s
ρ	Density kg m^{-3}
σ	Surface tension N m^{-1}
τ	Stress-strain tensor Pa

Dimensionless groups

Eo	Eötvös number
Fr	Froude number
M	Morton number
Re	Reynolds number
Sh	Sherwood number
Sc	Schmidt number

of microorganisms and on the operational conditions, the biofilm presence allows the removal of several nutrients and organic matter and are also capable of entrapping pathogens from the wastewater. Reactors with biofilm need less space, have a reduced hydraulic retention time and also present some resilience to changes in the environment (Sehar and Naz, 2016). For waters with a high content of organic matter and nutrients (like the ones from swine manure), the conventional methods of treating this type of contamination demand a high oxygenation, which becomes expensive (González et al., 2008). Oxygen is fundamental to control biofilm growth and maturation: in aerobic systems, the oxygen concentration is the limiting factor for biofilm growth, while in anaerobic systems, the presence of oxygen can severely compromise the survivability of the existing species. In aerobic systems, the lack of oxygen seems to shut down fiber production which is essential to the microorganism wall adhesion (Floyd et al., 2015) and, for *Escherichia coli*, its absence seems to be sufficient to prevent biofilm development (Colón-González et al., 2004). In contrast, *Pseudomonas aeruginosa* forms more robust biofilms in anaerobic systems with a higher thickness and a higher number of living organisms (Yoon et al., 2002).

The best way to control biofilm growth is by preventing the definitive adhesion of cells to the tube/container wall. The fact that the movement of Taylor bubbles drastically changes the hydrodynamic conditions on its surroundings, namely the wall shear stress, can be very useful for this purpose. In contrast to this preventing/cleaning action, when it is necessary to provide gaseous reactants/inhibitors to maintain biofilms, Taylor bubbles are an excellent transport medium.

Compared with single-phase flow, the use of gas–liquid slug (Taylor bubbles) flow has proven itself capable of enhancing the surface cleaning process (Aramrak et al., 2011; Cui et al., 2003; Ghosh and Cui, 1999; Ratkovich et al., 2013; Silva et al., 2017) due to several interrelated effects acting via three different phenomena:

- 1 Increased wall shear stresses promoted by slug flow (Ghosh and Cui, 1999) (hydrodynamics effects);
- 2 Higher mass transfer coefficients from the wall to the liquid flowing around the bubble (Silva et al., 2017) (mass transfer effects);
- 3 Availability of soluble gas to be transferred from the bubble to the liquid and, after, reaction with the soluble component to consume accumulated matter in the walls (mass transfer and reactive effects).

In this work, oxygen mass transfer from a Taylor bubble to the surrounding flowing liquid in a conventional scale vertical tube was studied using computational fluid dynamics (CFD) techniques. The main objective is to predict the gas–liquid mass transfer coefficients from the gas to the liquid phase. In future works, this knowledge can be used to estimate the oxygen flux that reaches biofilms attached to the tube wall. These results will reveal the conditions where biofilm development will be enhanced or inhibited. The quantity of solute available in the liquid can be controlled by the number of bubbles per unit time. The bubble composition will also have a crucial role to control gas–liquid mass transfer on these systems, i.e. the amount of dissolved oxygen is crucial for aerobic system, while its presence can be harmful to anaerobic biofilms.

Regarding the paper contents, firstly, there is a brief description of several important concepts in order to justify the chosen conditions as well as to help the interpretation of the obtained results. In the second part, the methodology used is described and it is followed by the

report and discussion of results. Finally, some overall conclusions are presented.

2. State of the art

2.1. Slug flow regime

In vertically oriented systems where gas and liquid are rising together, slug flow is one of the four major flow patterns alongside bubbly, churn and annular flows (Taitel et al., 1980). The main characteristic of slug flow is the presence of long and wide gas bubbles, occupying almost all the cross-section of the tube, also known as Taylor bubbles. These bubbles are generally followed by liquid slugs that can have entrapped small bubbles, especially for large tubes with liquid flowing at high Reynolds numbers.

To predict and analyze the hydrodynamics surrounding a Taylor bubble flowing through a stagnant liquid, the properties of the fluids (viscosity (μ), density (ρ), and surface tension (σ)) and the geometric parameters (diameter (D) and orientation of the tube) must be taken into consideration. The best way to do it is by defining typical dimensionless numbers (Araújo et al., 2012; Fabre and Line, 1992; Nogueira et al., 2006b, 2006a; Taha and Cui, 2006) that account for the main forces involved:

- Morton number, $M = \frac{g\mu_L^4(\rho_L - \rho_G)}{\rho_L^2\sigma^3}$;
- Eötvös number, $Eo = \frac{g(\rho_L - \rho_G)D^2}{\sigma}$;
- Froude number, $Fr = \frac{U_\infty}{\sqrt{gD(\rho_L - \rho_G)/\rho_L}}$.

where U_∞ is the Taylor bubble velocity in a stagnant liquid.

When the liquid starts to flow co-currently, the bubbles velocity changes. Nicklin et al. (1962) studied Taylor bubbles flowing in co-current with water and concluded that the bubbles velocity is well described by:

$$U_B = U_\infty + c\bar{U}_L \quad (1)$$

where U_∞ is the velocity of the bubble rising through stagnant liquid, \bar{U}_L the average liquid velocity and c a parameter that has a value of 1.2 or 2, depending if the liquid flow regime is turbulent or laminar, respectively.

It is then necessary to add another dimensionless group that accounts for the inertial effect of the liquid flow:

- Reynolds number, $Re_B = \frac{\rho_L U_B D}{\mu}$.

In columns with vertical orientation, and according to Eq. (1), Taylor bubbles rise faster, due to the buoyancy effect, displacing and overpassing the liquid.

The mass transfer is closely linked to the flow conditions. Around the bubble, different hydrodynamic regions develop:

- The bubble round front is known as the bubble nose. Dumitrescu (1943) was one of the firsts to study experimentally, through photographs, and theoretically, applying the potential flow theory, the shape of the nose of a Taylor bubble rising through stagnant water contained in a vertical tube. Nicklin et al., (1962) assessing two-phase slug flow in vertical columns of stagnant and co-current flow of liquid, suggested that the oblate spheroidal front of a Taylor bubble is only dependent on the flow conditions ahead of it, namely the liquid velocity field and viscosity. Close to the bubble nose, the liquid acquires radial velocity and starts moving

downwards around the bubble (in a frame of reference moving with the bubble-MFR), promoting the formation of a liquid film between the bubble surface and the wall;

- The liquid displaced continues to flow downward (MFR) through the annular space between the bubble and the tube wall. As the liquid flows further, the film boundary layer, initially adjacent to the tube wall, grows in order to occupy the entire annular space between the bubble and the wall. When this boundary layer reaches the surface of the bubble, a film of stabilized thickness and velocity profile is reached. Since the pressure adjacent to the film is constant – a consequence of the constant pressure in the interior of the gas bubble – the gravitational forces acting on the liquid film are balanced by both the shear stress at the wall and at the gas-liquid interface and the liquid is in a free falling flow. The larger the Morton number, the thicker is this developed film. The statement of a value for the transition from laminar to turbulent regime in a developed film around a Taylor bubble is not consensual in the literature. This difficulty is most of the times associated to oscillations in the bottom of the bubble. Nevertheless, the most referenced value is given by Fulford (1964):

$$400 < Re_f = \frac{\rho_L \bar{U}_f \delta_H}{\mu} < 800$$

where Re_f is the Reynolds number in the film, δ_H the film thickness and \bar{U}_f the average liquid velocity in the film.

- At the bubble tail, the liquid expands around or into a liquid wake. One of three kinds of wakes can be observed depending on the liquid flow regime in this region (Campos and Guedes de Carvalho, 1988). The first, for laminar regime, is a closed axisymmetric toroidal wake where the liquid flows upwards attached to the bubble tail. The second, for transitional regime, is a closed non-axisymmetric wake. Along the bubble path, there are periodic detachments of recirculation vortices, giving rise to a kind of von Kármán vortex sheet. Finally, there is an opened wake where irregular turbulent eddies appear and remain active at several diameters below the bubble tail – turbulent regime. This latter type of wake does not have a clear boundary. Further below the wake, the liquid recovers its undisturbed conditions, i.e., it flows with a profile similar to the stabilized liquid ahead the bubble nose.

Based on the work of Campos and Guedes de Carvalho (1988); Pinto et al. (1998) suggested the following limits for the flow patterns in the wake of a Taylor bubble rising co-currently with the liquid phase:

$$\text{Laminar wake} - Re_v = \frac{\rho_L \bar{U}_L^{MFR} D}{\mu} < 175$$

$$\text{Transitional wake} - 175 < Re_v = \frac{\rho_L \bar{U}_L^{MFR} D}{\mu} < 525$$

$$\text{Turbulent wake} - Re_v = \frac{\rho_L \bar{U}_L^{MFR} D}{\mu} > 525$$

where Re_v represents the Reynolds number with the average liquid velocity, \bar{U}_L^{MFR} , expressed in a reference frame moving with the bubble.

2.2. Mass transfer from a bubble into the surrounding liquid

2.2.1. Theoretical models and experimental works

The mass transfer mechanism of a soluble component from a Taylor bubble to the liquid is sluggish when compared with the liquid convective transport around the Taylor bubble interface. This time-scale lag increases as the fluid viscosity and diffusivity of the component in the liquid decrease. From this fact, many of the studies of mass transfer around Taylor bubbles were towards creating models based on the penetration theory of Higbie.

Higbie (1935) proposed the penetration model in order to predict the mass transfer during gas absorption. This model assumes that the liquid surrounding the interface is composed by several small units which are constantly renewed by the bulk liquid flow. The model assumes unsteady mass transfer from the gas to a liquid element, as long as this element is in contact with the gas. All the liquid elements are in contact with the gas during the same period of time and, at the interface, there are thermodynamic equilibrium conditions.

According to the model, the mass transfer rate, N_A , at instant t is given by:

$$N_A = A \sqrt{\frac{D_L}{\pi t}} (C_{A,i} - C_{A,\infty}) \quad (2)$$

The model assumes a mass transfer coefficient, k_L , defined as:

$$k_L = \sqrt{\frac{D_L}{\pi t}} \quad (3)$$

where D_L denotes the solute diffusion coefficient in the liquid phase, $C_{A,i}$ stands for the solute concentration at the interface, A is the interfacial area, while $C_{A,\infty}$ represents the concentration in the liquid bulk.

If the contact time is t_c (time that a particle takes to travel along the bubble surface), the average mass transfer coefficient during this time interval is then given by:

$$\bar{k}_L = 2 \sqrt{\frac{D_L}{\pi t_c}} \quad (4)$$

This theory has the contact time as the principal contributing factor and assumes that $\bar{k}_L \propto D_L^{1/2}$, as in every laminar diffusion process.

Mass transfer is highly dependent on the hydrodynamic characteristics of the flow (Treybal, 1981). Therefore, the distinct flow regions surrounding a Taylor bubble, described above, will have different effects on the solute transfer rate from a moving bubble to the flowing liquid. Some experimental studies have already tried to establish mass transfer correlations taking into account the penetration theory and the specificities of these hydrodynamic regions.

van Heuven and Beek (1963) measured the liquid-side mass transfer coefficient for Taylor bubbles of carbon dioxide rising in narrow tubes (diameter between 2.4–4.8 mm) filled with water. These authors adapted the theory of Higbie (1935) to describe adequately the absorption process. It was assumed that, for a long bubble rising in a quiescent liquid, the mass transfer is set not only by the potential flow in the bubble nose region but also by the developed laminar liquid film flowing around the Taylor bubble. Accordingly, the mass transfer

coefficient was expressed by the following equation:

$$\bar{k}_L A = 4(\pi D_L)^{1/2} (g/D)^{1/4} D^2 \left[I(l/D) + (g/D)^{-1/2} \frac{\left(\frac{D}{2} - \delta_H\right)^2}{D} (u + U_B) \frac{L_S - l}{D} \right]^{1/2} \quad (5)$$

where \bar{k}_L is the average liquid side mass transfer coefficient, A the Taylor bubble interfacial area, D_L the solute diffusion coefficient, g the gravitational acceleration, D the tube diameter, δ_H the stabilized liquid film thickness, u the liquid velocity at the interface in the stabilized film, U_B the rising bubble velocity, L_S the Taylor bubble length, l the distance between the nose tip and the axial location where the liquid film reaches fully development, and, finally, $I(l/D)$ represents a function that can be solved through the bubble shape consulting the work of Clift et al. (1978).

Filla (1972) and Niranjana et al. (1988) measured the mass transfer coefficient from a rising CO_2 Taylor bubble to stagnant water. Niranjana and colleagues used also others liquids such as glycerol-water solutions and aqueous carboxymethyl cellulose (CMC) solutions to investigate the effect of the fluid properties on the mass transfer. Both authors correlated their data and obtained similar expressions:

$$\bar{k}_L A = 4.59 D D_L \left(\frac{U_B D}{D_L} \right)^{1/2} \left(\frac{L_S}{D} \right)^{0.8} \quad \text{Filla correlation} \quad (6)$$

$$\bar{k}_L A = 2.6 D D_L \left(\frac{U_B D}{D_L} \right)^{1/2} \left(\frac{L_S}{D} \right)^{0.96} \quad \text{Niranjana correlation} \quad (7)$$

These equations have a limited range of applicability, since they only give satisfactory approaches for Taylor bubbles flowing through stagnant liquids and for $L_S/D < 8$. Besides, Filla correlation should only be used when the liquid is water.

The experiments of Filla (1972) and Niranjana et al. (1988) seem to confirm the theoretically predicted proportionality between \bar{k}_L and $D_L^{1/2}$. However, they also point to an almost independency between \bar{k}_L and the bubble length, L_S , in the range $2D < L_S < 8D$. This conclusion is surprising on the light of the penetration theory. Indeed, according to this theory, in long Taylor bubbles, the contact time of an element of fluid flowing around it increases and by consequence a decrease in \bar{k}_L would be expected (Eq. (3)). This will be a point to clarify in the present work.

Sena Esteves and Guedes de Carvalho (1993) presented an experimental study based on a simplified method to obtain the volumetric mass transfer coefficients for long bubbles flowing through different liquids in tubes with a diameter between 19–32 mm. The authors also compared their results with data from van Heuven and Beek (1963); Filla (1972) and Niranjana et al. (1988). The data obtained compared well with the theoretical predictions of van Heuven and Beek (1963). A simple asymptotic expression, based on van Heuven and Beek equation, for the evaluation of average mass transfer coefficients in long Taylor bubbles (i.e. Taylor bubbles with a fully developed film along a large portion of the total length) was also established by the authors:

$$\bar{k}_L A = 2 \sqrt{\frac{D_L (u + U_B)}{\pi L_S}} [\pi (D - 2\delta_H) L_S] \quad (8)$$

where u is the liquid velocity at the bubble interface.

Kreutzer et al. (2001) proposed, and experimentally validated, a model that takes in consideration the sequential steps involved on the mass transfer from the gas bubble to the wall, i.e., solute transfer from the bubble into the liquid film and from the liquid film into the wall. However, to apply their model, it is necessary to know the thickness of the developed liquid film, the liquid slug length and also the superficial gas and liquid velocities.

Other experimental studies about mass transfer in Taylor bubbles were performed with different aims.

Hosoda and colleagues (Hosoda et al., 2015, 2014) experimentally studied the dissolution of CO₂ Taylor bubbles in vertical pipes. In the first study, the bubble was rising in a stagnant liquid (2014) and, in the following (2015), the bubble was steady in a downward flow of water or glycerol-water solutions. In both, it was used an image processing method.

In the literature, there are also several articles on this topic in small tubes (milli and microchannels). But in these cases, the surface tension has an important effect overlapping that of gravity.

Although there are several correlations to predict mass transfer, the majority do not allow the quantification of the local mass transfer coefficients around the bubble (nose, film and tail/wake regions) and most of them are valid only for stagnant liquid conditions. Furthermore, the applicability of the penetration theory is another subject that remains open and will be carefully evaluated in this work.

2.2.2. Numerical studies

There are two main approaches to numerically solve a mass transfer problem in a two phase flow scenario. In the first approach, averaged governing equations for the mass transfer are used in parallel with empirical correlations for computing the gas–liquid interphase mass transfer coefficients. The solution is therefore limited by imposed assumptions. The second approach implies a coupled solution of the two phase flow and the species conservation equation. The species conservation equations are solved in each element of the simulation domain, while the interface is determined by proper interface defining methods. This approach requires, most of the times, adequately fine grids and sufficiently small time steps, and thus, the computational time is very high, in particular for highly viscous fluids (high values of Morton and Schmidt numbers).

To reduce the overall grid resolution required, there are, in the literature, alternatives to the integral resolution of the conservative equations. For example, Aboulhasanzadeh et al. (2013, 2012) used a boundary-layer approximation next to the bubble and a relatively coarse grid for the rest of the flow.

There are different methods developed to numerically define the interface in a gas–liquid flow: Level Set based method (Deshpande and Zimmerman, 2006), Front-Tracking method (Darmana et al., 2006) and Volume of Fluid method (VOF) method (Davidson and Rudman, 2002). VOF method is one of the most used to identify gas–liquid interface for Taylor bubble flows. However, it presents some problems on solving the mass transfer at the interface. At the cell scale, the interface presents some “diffusion” for the value of the phase volumetric fraction (α) which makes the concentration field calculation more difficult, particularly, when the concentration gradients are high.

In addition to this numerical diffusion, there is also the complexity introduced by the solute interfacial discontinuity governed by the thermodynamic equilibrium in the solute

distribution between phases (Henry’s law). There are several works published in the literature on numerical procedures to solve this problem whether in spherical or in Taylor bubbles. Alke et al. (2009) proposed two alternatives: the equilibrium at the interfacial cells method and the concentration gradient method. Regarding the former, on cells that enclose the interface, the component that is being transferred is in equilibrium between mixed phases and a conservative redistribution of the molar species is imposed. In contrast, the concentration gradient method is based on the concentration gradients on the liquid phase adjacent to the interface. Hayashi and Tomiyama (2011) solved the discontinuity by using a temporal variable transformation of the concentration of the species and a harmonic mean of the diffusion coefficient. This method was later used by Hayashi et al. (2014) to study mass transfer from CO₂ Taylor bubbles to glycerol-water mixtures and to evaluate the effect of surface oscillations on the mass transfer.

2.2.3. Work developed accordingly the state of the art

According to the state of art, which include experimental and numerical works, there are still aspects not clarified with respect to the mass transfer of a solute from a Taylor bubble to the flowing fluid. As our ultimate goal is the application to biological systems, usually viscous, we intend to quantify mass transfer under laminar conditions, and so, for high values of Morton and Schmidt (Sc) numbers. The strategy chosen was to select specific conditions in terms of the dimensionless groups, solve the integral species conservation equations in an appropriate mesh (at the expense of long computational times), physically analyze the results and, based on this analysis, go to the establishment of averaged governing equations. This option will also allow the sustainability analysis of the experimental models established on the basis of the penetration theory.

To implement this strategy, some options have been taken and are briefly described below:

- The simulations were done with the commercial package ANSYS Fluent;
- The hydrodynamic simulations took advantage of the knowledge already gathered by the research group about hydrodynamics of two-phase flow systems (Araújo et al., 2012; Mayor et al., 2007a,b; Nogueira et al., 2006a; Mayor et al., 2008);
- The hydrodynamic simulations used the VOF method to delimit the interface;
- The transfer from an oxygen bubble to a flowing liquid (water-glycerol mixture) was studied. Since the bubble is a pure component, there is no internal resistance to mass transfer, and therefore the interface discontinuity is avoided;
- The volume variation of the bubble during the simulation time is a negligible fraction of the total volume.

In the following sections, the method will be presented in detail.

3. Material and methods

Mass transfer from a pure oxygen Taylor bubble to the surrounding liquid was numerically studied by performing simulations with different liquid velocities —Table 1.

Table 1 – Average liquid velocity, bubble velocity, bubble length and Re_B used to study mass transfer phenomena.

	\bar{U}_L (m.s ⁻¹)	U_B (m.s ⁻¹)	L_b/D	Re_B
CASE0	0.000	0.38	2.0	83
CASE1	0.025	0.49	2.0	108
			2.1	
			3.5	
CASE2	0.050	0.59	5.5	133
			8.9	
			2.1	
CASE3	0.075	0.69	2.1	158
CASE4	0.100	0.78	4.1	185
			2.1	
CASE5	0.125	0.86	2.1	208

The system chosen is characterized by the following dimensionless numbers:

$$M = 5.30 \times 10^{-5}, \text{Eo} = 95 \text{ and } \text{Sc} = 1.84 \times 10^4.$$

The viscosity used was 0.045 Pa.s corresponding to a glycerin aqueous solution 82% v/v, while the diffusion coefficient of oxygen in this solution is $1.97 \times 10^{-9} \text{ m}^2 \text{ s}^{-1}$.

In order to minimize the computational time, but maintaining numerical accuracy, the simulations were divided into two successive steps, both performed in a FRF (fixed reference frame):

- Hydrodynamics step: rise of a single Taylor bubble through a co-current liquid in a vertical tube until the bubble acquires its final shape;
- Hydrodynamics plus mass transfer step: inclusion of the oxygen transfer from the Taylor bubble to the flowing liquid after the bubble reaches its definitive shape and the flow field surrounding the bubble gets stabilized.

The simulations were performed in an axisymmetric two-dimensional domain representing half of a cylindrical tube with a diameter (D) of $2.07 \times 10^{-2} \text{ m}$. The length of the tube was $15D$ to guarantee enough distance for the bubble displacement during the two consecutive simulation steps. Two different grids were used to acquire the hydrodynamic features as well as to study the mass transfer (validation mesh tests presented in Section 4.1). The meshes were created using Meshing software (component of the ANSYS Workbench) where the domain was uniformly split into quadrilateral control volumes imposing an aspect ratio of 1. The outlet boundary condition was defined as a pressure-outlet, where at the exit of the system the static pressure had a defined value. A no-slip condition was applied to the wall. At the inlet, a parabolic velocity profile was imposed assuming fully developed laminar flow in the liquid and Reynolds number between 0–73 considering the average liquid velocity.

The continuity (Eq. (9)) and momentum equations (Eq. (10)) applied are implemented on ANSYS Fluent 16.0:

$$\nabla \cdot (\rho \vec{u}) = 0 \quad (9)$$

$$\rho \frac{\partial}{\partial t} (\vec{u}) + \rho \nabla \cdot (\vec{u} \vec{u}) = -\nabla p + \nabla \cdot (\tau) + \rho \vec{g} + \vec{F} \quad (10)$$

where ρ represents the density, p is the static pressure, τ the stress-strain tensor, $\rho \vec{g}$ the gravitational forces and \vec{F} the external body forces.

To determine the location of the gas–liquid interface, the VOF (Volume of a Fluid) method coupled with a geometric

reconstruction scheme (Youngs, 1982) was used — Eq. (11). The geometric reconstruction scheme solves the interface through a piecewise-linear approach (PLIC) for the gas volume fraction (α_G).

$$\frac{\partial}{\partial t} (\alpha_G) + \vec{u} \cdot \nabla \alpha_G = 0 \quad (11)$$

Eqs. (9) and (10) are shared by both gas and liquid phases, while the viscosity and density (referred in Eq. (12) by ϕ) are weighted with the α -value.

$$\phi = \alpha_G \phi_G + (1 - \alpha_G) \phi_L \quad (12)$$

The continuum surface model (Brackbill et al., 1992) was chosen to solve the effect of the surface tension in the gas–liquid interface. The source term in the momentum equation incorporates this surface tension effect.

As described in previous works (Araújo et al., 2012; Silva et al., 2017): the PISO (“Pressure-implicit with splitting of operators”) was used to couple velocity and pressure equations; for the momentum equation, the “QUICK” method was employed as interpolation scheme; for the pressure interpolations, the PRESTO! scheme was chosen. The gradients of the scalars were computed through the Green-Gauss method. The implicit body force treatment was used to prevent convergence problems and guarantee robust solutions. The description and details of all these methods and schemes can be found in (“ANSYS FLUENT Theory Guide,” 2011).

The simulations time step was variable and controlled by a maximum Courant number of 0.25. As the convergence criterion for each time step, the values of the residuals for momentum and continuity equations were monitored and set lower than 10^{-6} .

3.1. Hydrodynamic simulations

To obtain the stabilized velocity fields and the final bubble shapes, a first set of simulations was performed on a mesh with 52×1560 elements. This mesh density was previously validated to solve the hydrodynamic flow of single Taylor bubbles (Araújo et al., 2012; Silva et al., 2017). All simulations were initialized with a quarter of a circle (the bubble nose), linked to a rectangle with a width equal to the radius of the circle (the bubble body). The bubble was initially placed near the tube inlet (bottom of the computational domain) and it was allowed to move upwards through the tube with a stationary wall (FRF). The simulations ran until the bubble reached a stabilized form.

3.2. Mass transfer studies simulations

Mass transport was solved through the “species transport” model implemented in ANSYS Fluent 16.0. The local mass fraction of i^{th} specie (y_i) was determined by solving the mass conservation equation:

$$\frac{\partial}{\partial t} (\rho y_i) + \nabla \cdot (\rho \vec{u} y_i) = -\nabla \cdot \vec{J}_i \quad (13)$$

where \vec{J}_i represents the diffusive flux of species i .

Imposing a constant concentration at the gas–liquid interface is a challenging task especially when using ANSYS Fluent. This software requires mass transfer rates as boundary conditions. To solve this issue, a new boundary condition

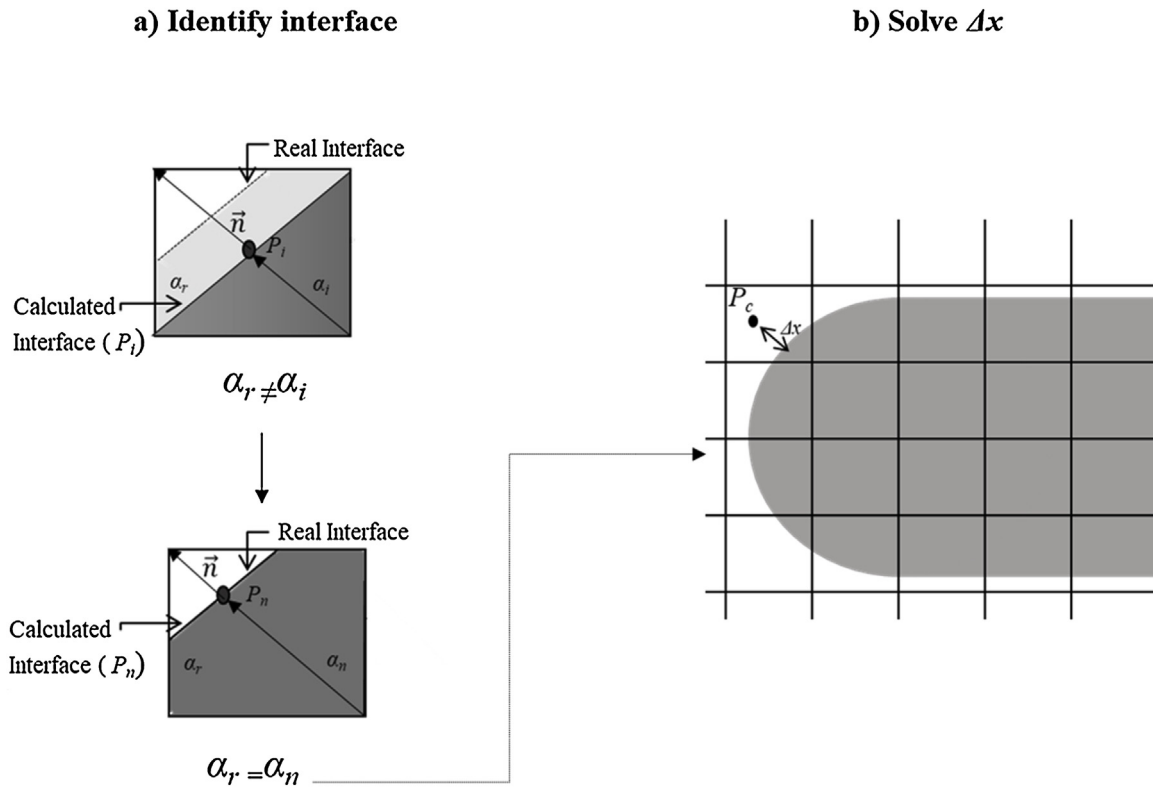


Fig. 1 – (a) Schematic representation of the interface determination; (b) Schematic representation of the interface cells and of ΔX calculation based on the work of Özkan et al. (2016).

was implemented through a user-defined function subroutine (UDF) as a source term. This boundary condition, the mass transfer rate at the interface N_A , was defined as:

$$N_A = -\nabla c D_L A \quad (14)$$

where A stands for the interfacial area (it can be calculated for each cell by multiplying the cell volume by the magnitude of the void fraction gradient, Özkan et al. (2016)) and ∇c is defined as:

$$\nabla c = \frac{c^* - c_{dis}}{\Delta X} \quad (15)$$

where c_{dis} is the concentration on the cell center next to the interface. A solubility of $8.0 \times 10^{-3} \text{ kg m}^{-3}$ (c^*) was considered and imposed at the gas–liquid interface.

While all the other variables are easy to impose or get directly from the software, setting the distance between the interface and the cell center (P_c), ΔX , is the main issue, particularly in regions with curvature. Özkan et al. (2016) described a method to solve this problem. In this method, ΔX is calculated through the liquid void fraction and through the interface normal vectors coming from the VOF-PLIC scheme. Next, a brief description of this method is provided.

The first step to obtain ΔX is to set the interface. The normal vectors and α_r (which dictates the phase volume) are retrieved from ANSYS Fluent. A simultaneous code first assumes a point (P_i) along the normal vector direction to belong to the interface. The code uses this point to set a calculated interface. The correspondent phase volume (α_i) is then calculated and compared with the value acquired from ANSYS Fluent. If these values are congruous, the program stops and ΔX is computed. If not, the position of the point is changed, along the normal vector, and a new point is considered (P_n). Once again the correspondent

phase is calculated (α_n). This process repeats itself until α_n is equal to α_r — Fig. 1.

The flow field to perform mass transfer simulations was obtained through an interpolation of the pressure and velocity components to a denser grid (100×3000 cells). When the simulation starts, the bubble shape was already stabilized and oxygen only existed inside the bubble.

As already mentioned, simulations were performed for a set of different liquid velocities. The average velocity of the parabolic profiles imposed at the inlet varied between 0 and 0.125 m s^{-1} . This corresponds to a Re_B between 83–208.

In all simulated systems, the bubble rise was stopped once the oxygen distribution stabilized in the close surroundings of the bubble. Local mass transfer coefficients were determined along the bubble interface for over 30 positions which included the nose, film and tail-wake regions. Then, a global mass transfer was calculated by averaging the local coefficients along the bubble surface.

4. Results and discussion

In the current section, the main results of this work are presented and discussed. First, the mesh independence tests are briefly described. Then, in the following sub-section, the mass distribution around the bubble, as well as the gas–liquid mass transfer coefficients, are discussed and compared with correlations available in the literature. Finally, the conclusions of this study are extrapolated to become wide-ranging.

4.1. Mesh tests

In order to guarantee an accurate prediction of the mass transfer data, mesh tests were performed for the system with an average velocity of $\bar{U}_L = 0.025 \text{ m s}^{-1}$. Different uniform

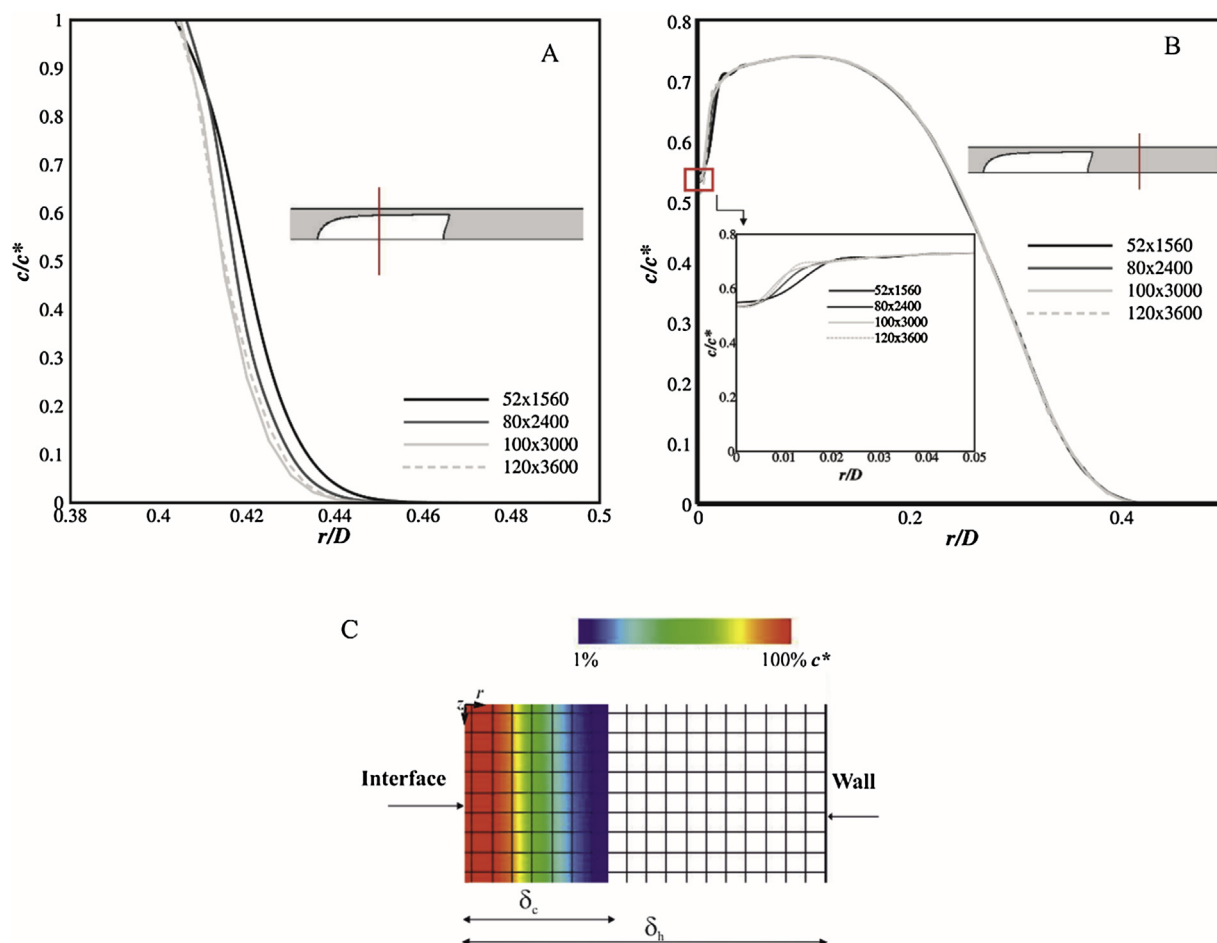


Fig. 2 – Radial dimensionless concentration profiles at two different axial locations: in the film region (A) and below the bubble (B) (each one represented by the red line on the figure scheme of each plot), acquired with different mesh densities. In part C of the figure, is shown the concentration distribution inside the mass boundary layer along the liquid film together with the corresponding mesh cells (mesh with 100×3000 cells). The concentration (δ_c) and the hydrodynamic (δ_h) boundary-layer thicknesses are represented for the system where $\bar{U}_L = 0.025 \text{ m s}^{-1}$ ($M = 5.3 \times 10^{-5}$, $Sc = 1.84 \times 10^4$ and $Re_B = 108$) (For interpretation of the references to colour in this figure legend, the reader is referred to the web version of this article).

meshes with a cell aspect ratio of 1 were tested: 52×1560 ; 80×2400 ; 100×3000 and 120×3600 cells. The option for the lower density (52×1560) comes from literature (Araújo et al., 2012), which states that this mesh is capable of correctly predicting the hydrodynamics in the conditions under study ($M = 5.30 \times 10^{-5}$ and $Eo = 95$).

In Fig. 2, radial dimensionless concentration profiles at the bubble level (A) and below the bubble wake (B) are presented for the tested meshes. At the bubble level, the concentration profile is much more sensitive to the mesh density and only the two denser meshes have almost overlapped results. Below the bubble wake, the differences between the concentration profiles obtained with the different meshes are negligible.

It is possible to conclude that the mesh with 100×3000 cells, which leads to a total of 300000 elements in the domain, is dense enough to accurately simulate the mass transfer phenomena on the kind of systems addressed in this study.

As previously mentioned, the fact that the liquid viscosity is high implies that the mass boundary layer is very thin. The mesh has to guarantee a sufficient number of cells inside this layer to assure an accurate concentration field. As can be seen in Fig. 2C, in the mesh chosen there are about 8 cells along the radial direction within the mass boundary layer developed in the liquid film region. So, this mesh density is enough to have

a proper and accurate definition of the concentrations inside the referred layer.

After defining an adequate mesh density, the influence of liquid velocity on the oxygen mass transfer was inspected and a compilation of results is presented in the following sub-sections.

4.2. Mass distribution around the bubble

4.2.1. Solute distribution

In Fig. 3, sequential concentration fields are represented, as an example, for the system with $\bar{U}_L = 0.025 \text{ m s}^{-1}$ to evidence the corresponding temporal evolution (starting from the initial moments when the mass transfer is activated). An image with the streamlines around the bubble was also added to Fig. 3.

At the bubble nose, the mass diffuses outwards up to a small distance from the bubble surface and quickly reaches a pseudo-stationary state i.e. the concentration field in the close surroundings of the bubble becomes time independent. Moving downwards along the bubble, in the film region, the pseudo-stationary concentration state is also reached after a few tenths of a second (physical time). The zone that demands more time to stabilize is the bubble tail-wake. In the liquid toroidal vortex, there is a slow accumulation of solute by

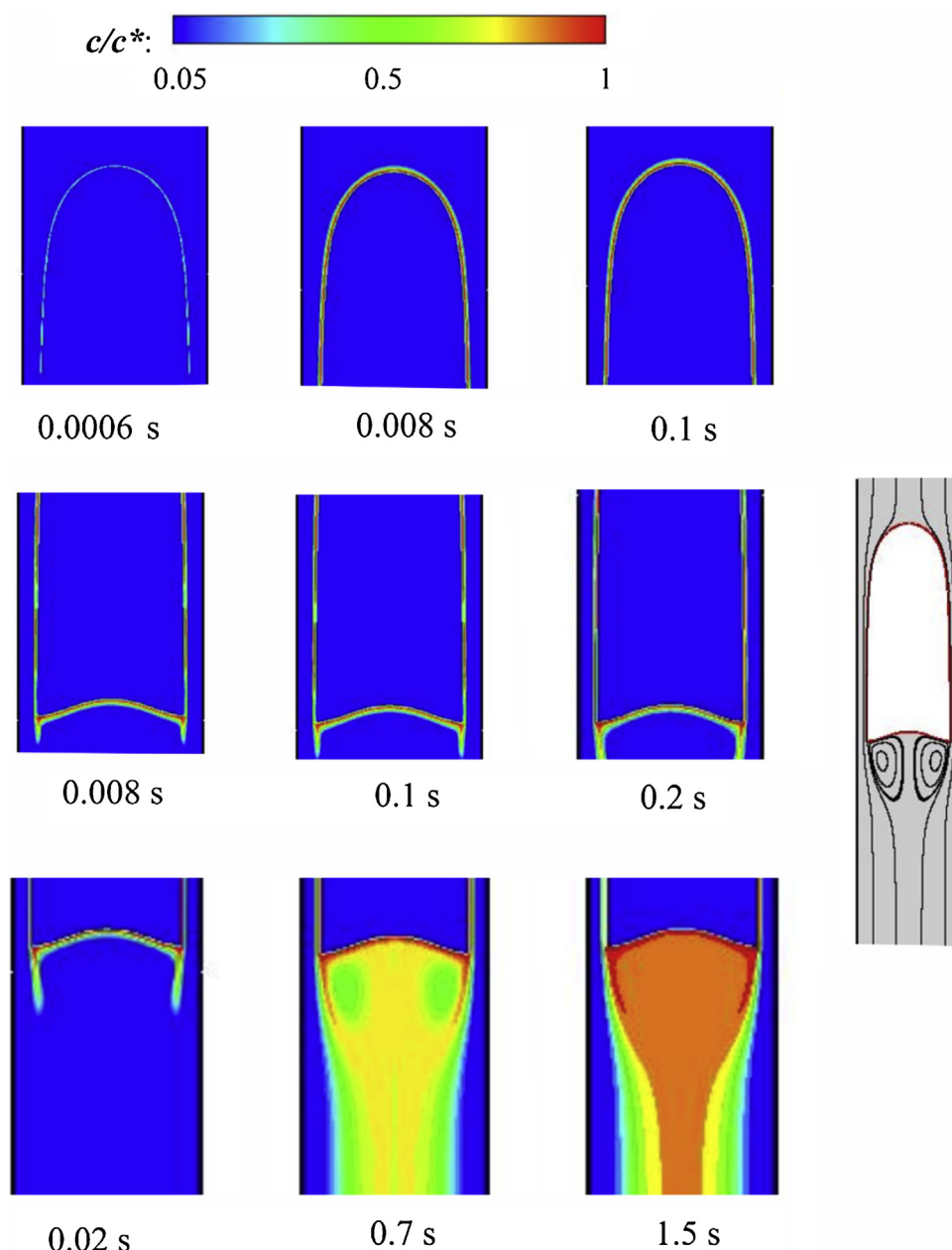


Fig. 3 – Representation of the concentration contours in the nose, film and tail regions for different moments until reaching a pseudo stationary-state. The results were obtained for a system with $\bar{U}_L = 0.025 \text{ m s}^{-1}$ and a bubble length of $2.01D$. An image with the streamlines around the bubble is also shown ($M = 5.3 \times 10^{-5}$, $Sc = 1.84 \times 10^4$ and $Re_B = 108$).

diffusion, retarding the complete definition of the stabilized concentration field around the bubble.

While the amount of solute in the nose and film regions is restricted to the close neighborhood of the bubble interface the liquid wake with its rising movement following the bubble tail, stores part of the solute dispersed.

The streamlines around the bubble allow to better understand the way mass is distributed around it, particularly inside the vortex where the combined rising and rotational movements (visible in a MFR- Moving Frame Reference) allow the upward transportation of solute.

The closed laminar wake (MFR) that flows together with the bubble begins to be fed with solute coming both from the film and after from the bubble tail. This process is slow and, as can be seen in Fig. 3, it takes about 1.5 s until the wake is saturated (for the conditions referred to in the legend). When a pseudo-stationary state is reached, there should be no accumulation of mass inside the wake, i.e., the mass that is coming

from the bubble tail should be the same that is transferred from the wake region to the flowing liquid in its surroundings. Because of this extended zone of higher concentration, as will be addressed below, the mass transfer coefficients in the tail are low.

In Fig. 4A, the axial dimensionless concentration profiles in the liquid flowing around the bubble are presented for three different radial positions. Starting from the bubble nose region, the oxygen concentration in the liquid phase increases in the downward direction, reaches its maximum value in the film and decreases near the tip of the bubble tail. As the radial positions approach the wall and get further away from the gas-liquid interface, the solute concentration in the liquid sharply decreases.

Following the concentration of a particle as it moves around the bubble, i.e. along a streamline, can also be insightful. Starting from an initial position (P.I), the concentration along four streamlines (s) is represented on Fig. 4B. The pro-

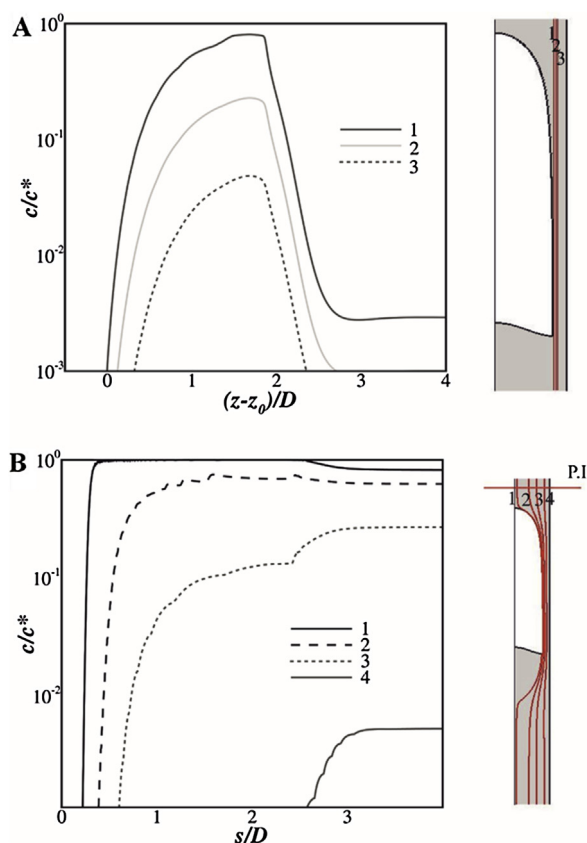


Fig. 4 – (A) Dimensionless oxygen concentration in the liquid along the axial direction for three radial positions (z_0 corresponds to the axial coordinate of the bubble nose tip). (B) Dimensionless concentration of oxygen along streamlines around the bubble. The coordinate s along the streamlines starts at the P.I plane (see representation in the right side). These numerical results correspond to a physical time of 1.5 s with $\bar{U}_L = 0.025 \text{ m s}^{-1}$ and a bubble with 2.01D ($M = 5.3 \times 10^{-5}$, $Sc = 1.84 \times 10^4$ and $Re_B = 108$).

files were taken when the concentration around nose and film regions no longer changed over time ($\Delta t = 1.5 \text{ s}$). The streamline marked as 1 goes along the interface, and so, the concentration saturation value is reached quickly. There is a slight reduction on the concentration values as this streamline stops following the bubble interface and enters the wake region. The concentration along streamline 2 closely follows the previous one and presents a similar behavior. The streamline 4 is the one farther away from the interface and it is also the one where the concentration has the lowest values. In this streamline closer to the wall, contrary to those near to the interface, there is a solute concentration increase as it arrives to the wake region, which is due to the solute diffusion from the regions of higher concentration on the liquid vortices (identified in Fig. 3) and also from the liquid closer to the interface.

Regarding the nose region, dimensionless concentration plots in the normal direction to the bubble surface are shown in Fig. 5.

In the auxiliary image, a grey region limited by the line that corresponds to 1% of the saturation concentration (dashed line) and the interface (full line) is also represented. According to the profiles, this 1% mass boundary layer is thicker in front of the nose, decreasing for downward axial coordinates.

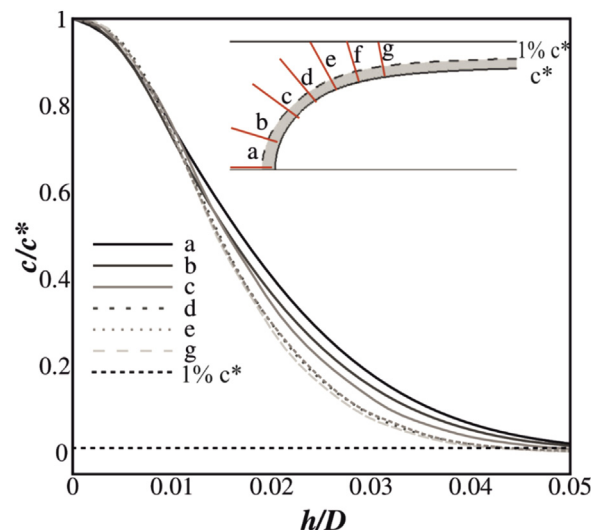


Fig. 5 – Dimensionless concentration of oxygen along h (distance from the bubble surface along the normal direction) for different positions around the bubble. A grey region limited by the line that corresponds to 1% of the saturation concentration (dashed line) and the interface (full line) is represented. This simulation has run for 0.5 s with $\bar{U}_L = 0.025 \text{ m s}^{-1}$ and a bubble with 2.01D ($M = 5.3 \times 10^{-5}$, $Sc = 1.84 \times 10^4$ and $Re_B = 108$).

This decrease is accompanied by an increase of the slope of the concentration profiles.

In Fig. 6, dimensionless radial concentration profiles are represented along the liquid film region. These profiles tend to be almost overlapped near the interface. Moving downwards through the film (z direction), a slight concentration increase occurs in inner positions of the mass boundary layer. This can be observed by comparing the augmented profiles in graphs for regions A and B of Fig. 6. Looking at the same Figure and based on the augmented profiles for region C, at the end of the mass boundary layer, it is verified an imperceptible increase of its thickness.

It should be noted that, in Fig. 6, the boundary layer of mass occupies about 30% of the thickness of the liquid film between the bubble and the wall.

4.2.2. Mass transfer coefficients

The values of the mass transfer coefficients along the bubble surface were determined from the raw numerical data. Two types of coefficients were considered: local (k_L) and average/global (\bar{k}_L) coefficients. The local coefficients were calculated using Eq. (16), along the normal directions at several locations throughout the bubble surface.

$$k_L = - \left[\frac{D_L}{c^* - c_{bulk}} \frac{dc}{dh} \right]_{h=0} \quad (16)$$

The average/global coefficients were obtained by integrating the local coefficients along the bubble surface. A distinction between average and global coefficients was defined: the average coefficients concern specific zones around the bubble, while the global mass transfer coefficients were calculated by integrating all the local values along the entire bubble surface.

From these average/global coefficients it was possible to estimate values for the average Sherwood number ($\bar{Sh} = \frac{\bar{k}_L L_S}{D_L}$).

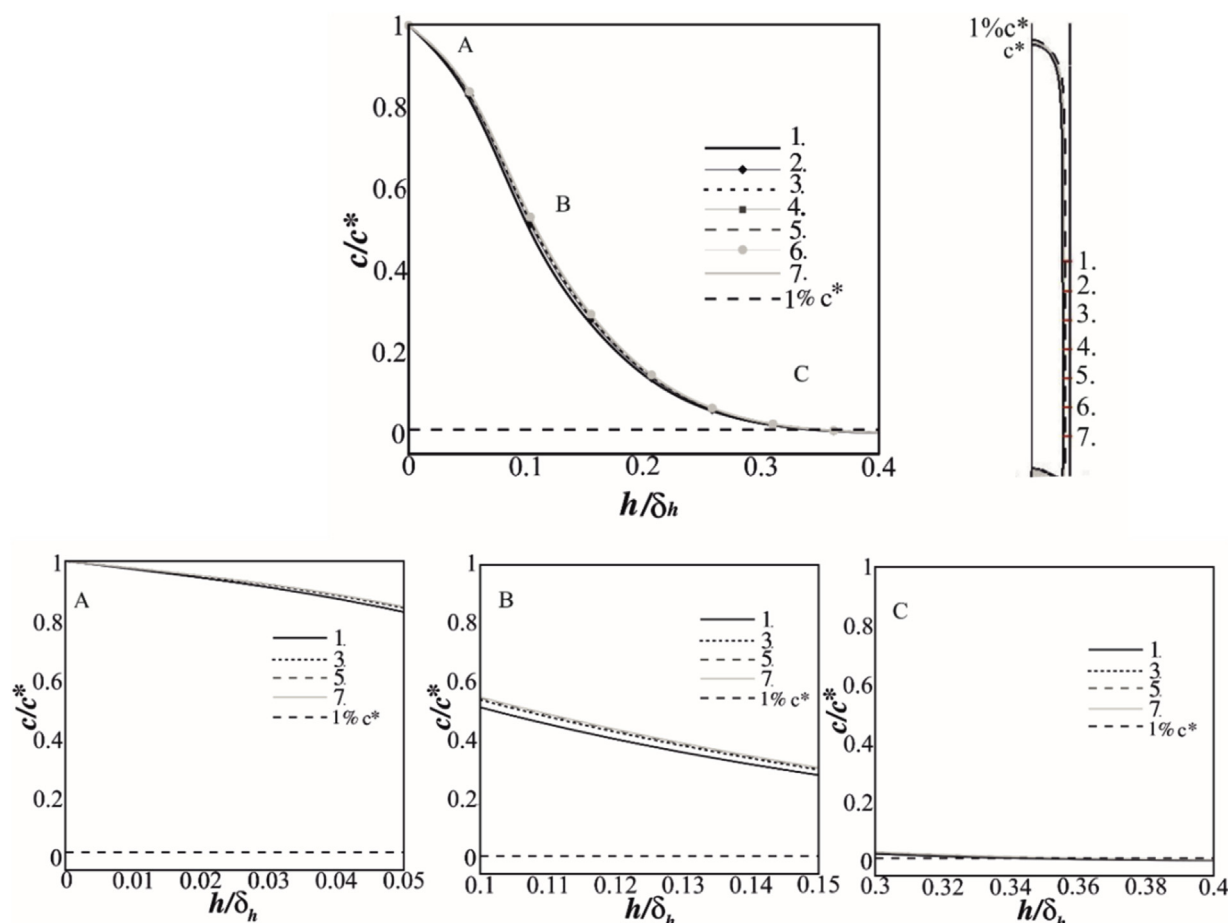


Fig. 6 – Dimensionless concentration of oxygen in the developed film region. The abscissas axis represents h (distance along the normal to the bubble surface), for different positions on the bubble film, normalized by the film thickness (δ_h). The corresponding axial positions as well as the line that represents 1% of the saturation concentration are schematically illustrated at the right side of the figure. This simulation has run for 0.3 s with $\bar{U}_L = 0.050 \text{ m s}^{-1}$ and a bubble with 5.5D ($M = 5.3 \times 10^{-5}$, $Sc = 1.84 \times 10^4$ and $Re_B = 133$). A zoom for three different regions along the concentration profiles is represented in the lower part of the figure.

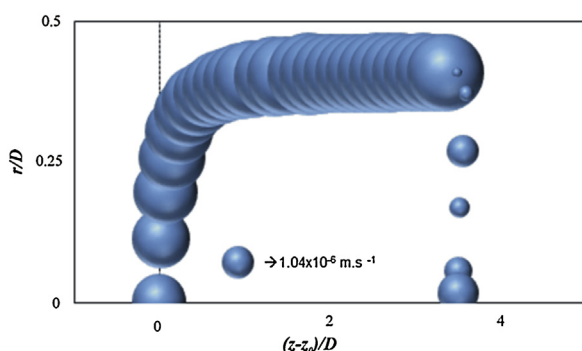


Fig. 7 – Local mass transfer coefficients along the bubble surface. Larger spheres indicate higher mass transfer coefficients. This simulation has run for 0.2 s with $\bar{U}_L = 0.050 \text{ m s}^{-1}$ and a bubble with a length of 3.5D ($M = 5.3 \times 10^{-5}$, $Sc = 1.84 \times 10^4$ and $Re_B = 133$).

For a qualitative visualization, the local mass transfer coefficients obtained for a system with $\bar{U}_L = 0.05 \text{ m s}^{-1}$ are represented in Fig. 7 along a bubble of length 3.5D. Each local coefficient is represented by a sphere: larger spheres represent higher mass transfer coefficients and vice-versa. It is possible to identify the tail as the region where the local coefficients present the lowest values. In opposition, the film region presents the highest mass transfer coefficients.

4.2.2.1. Bubble length effect on mass transfer coefficients. As referred in the introduction, Niranjana et al. (1988) concluded that \bar{k}_L and Taylor bubble length, L_S , in the range $2D < L_S < 8D$, are practically independent, which is a surprise considering the penetration theory. This conclusion was tested by simulating the mass transfer from bubbles with different lengths. In Fig. 8, local mass transfer coefficients data for increasing longer bubbles rising through liquids with $\bar{U}_L = 0.05 \text{ m s}^{-1}$ (A) and $\bar{U}_L = 0.10 \text{ m s}^{-1}$ (B) are shown.

From Fig. 8, it is possible to conclude that, for $(z - z_0)/D \geq 2$, the local mass transfer coefficients values tend to be constant.

Taking in consideration the thickness of the developed film, the length necessary to get the total development of the film was determined. For that, it was considered the axial distances from the nose (normalized by the column diameter) until the film reaches 95% of the developed film thickness. For all the cases studied, the film stabilization length was between 1.63D and 1.76D.

From Fig. 8 and the film stabilization length, it can be claimed that, around the value where the thickness of the film stabilizes, the local values of the mass transfer coefficient tend to the same value.

The values presented by Niranjana et al. (1988) are average values. However, the weight/relevance of the interfacial area of the film on the total interfacial area of the bubbles with $L_S > 2D$

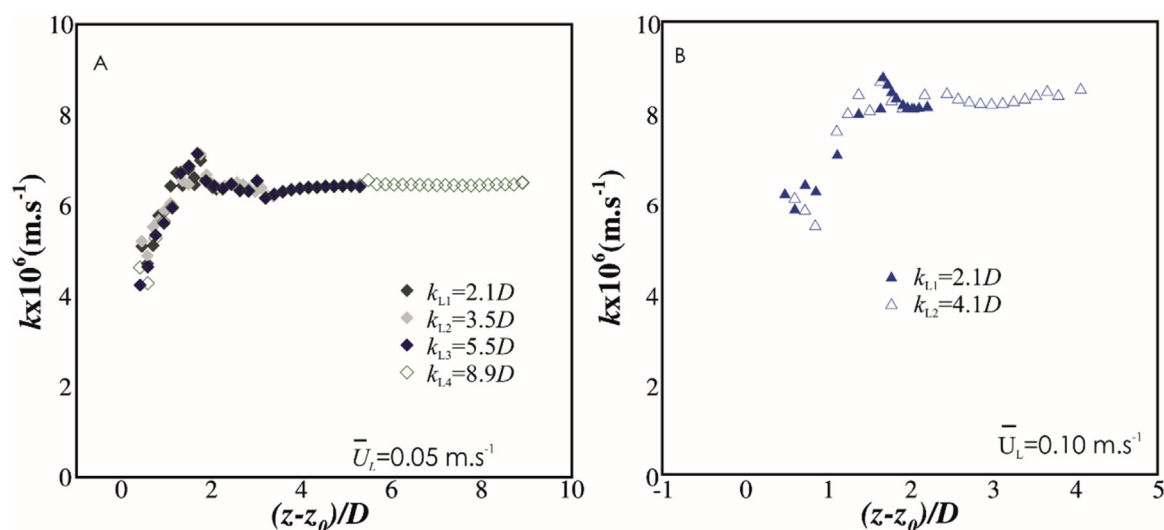


Fig. 8 – Local mass transfer coefficients along the film region obtained for different velocities and bubbles with different lengths. For $\bar{U}_L = 0.05 \text{ m.s}^{-1}$ (A), the bubbles have a length of 2.1D (1), 3.5D (2), 5.5D (3) and 8.9D (4). For $\bar{U}_L = 0.10 \text{ m.s}^{-1}$ (B), the shorter bubble has a length of 2.1D (1) while the longer has a length of 4.1D (2) ($M = 5.3 \times 10^{-5}$, $Sc = 1.84 \times 10^4$).

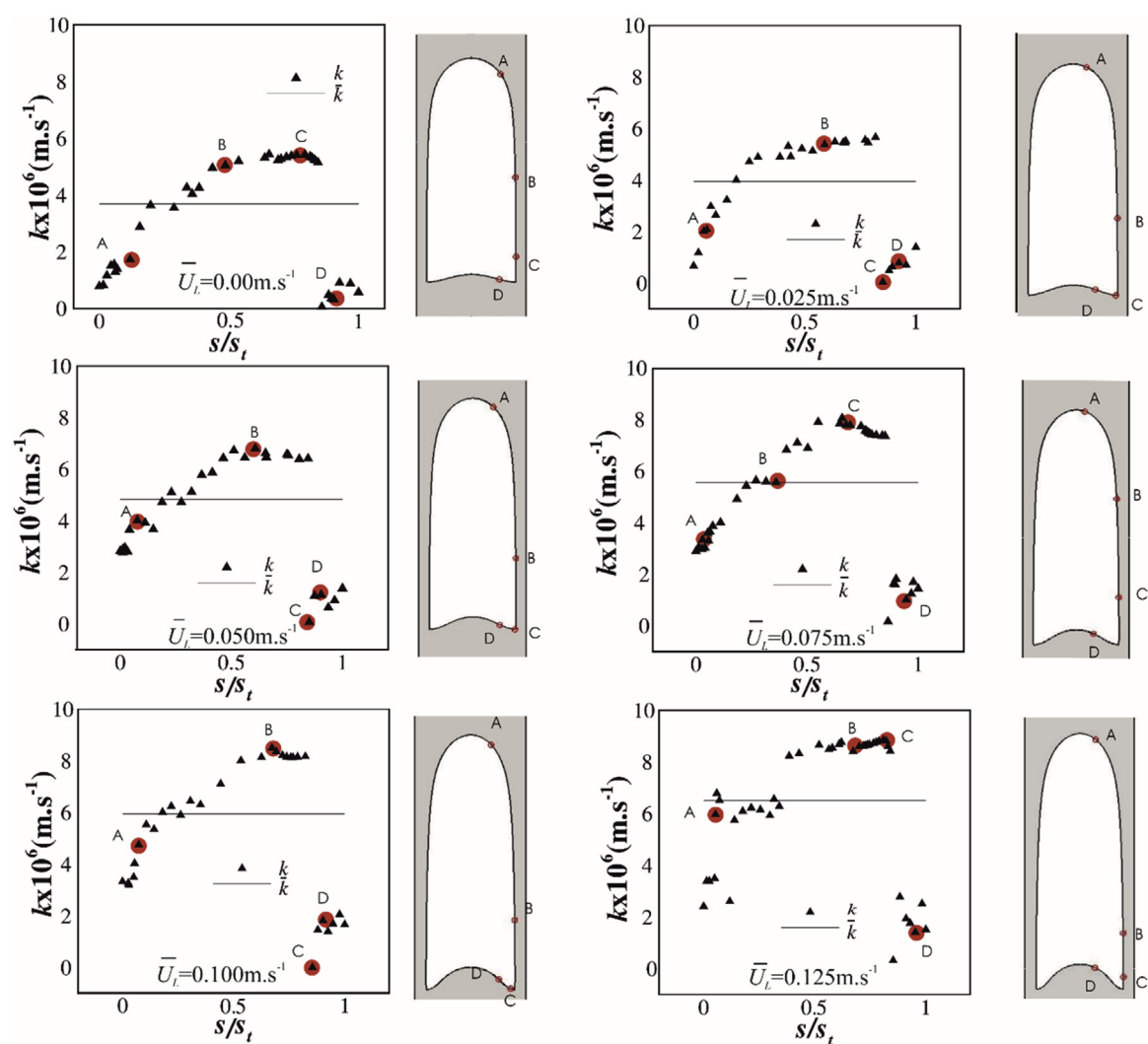


Fig. 9 – Local mass transfer coefficients along the bubble surface for different velocities. The dotted lines represent the global mass transfer coefficients. Next to each plot, a schematic representation of some positions is presented to help the interpretation of the plots ($M = 5.3 \times 10^{-5}$, $Sc = 1.84 \times 10^4$).

is irrefutable. Therefore, it can be concluded that, concerning the effect of bubble length, $L_S < 8D$, the trend observed in Fig. 8 is in agreement with the data of Niranjana et al. (1988).

To avoid the higher computational demands, from this point on, all the simulations addressed refer to bubbles with a length around $2.1D$. It should be noted that, even with this reduced bubble length, each simulation takes 2 months to reach 1.5 s using 1 node with 12 cores of a computer cluster (Avalanche — FEUP). This cluster is provided with 29 different machines, each one with an Intel® Xeon® Processor that varies between 2.00 and 2.50 GHz and access (on average) to 64 GB of RAM.

4.2.2.2. Average mass transfer coefficients along the different regions of the bubble. The local coefficients were studied in detail for the three different zones: bubble nose, developed film and bubble tail. As already noted, the average mass transfer coefficients were calculated from the integration of the local values. The local values were represented for the coordinate along the bubble surface (s) standardized by the bubble perimeter measured in the plane used to acquire the coefficients (s_t).

In Fig. 9, local and global coefficients are represented for different liquid velocities. For all velocities, the values of the coefficients increase along the bubble nose. As the hydrodynamic film becomes developed, the local mass transfer values tend to stabilize and, as expected from Fig. 7, this is the region where their values are higher. Regarding the tail region, the mass transfer coefficients are lower on the transition between the film and the tail. At the bubble bottom, these values increase until a radial position around the middle of the bubble radius, closer to the position above the eye of the recirculation vortex. After a decrease, there is another increase up to the tube center.

The slight perturbations/oscillations on the coefficient values, especially in the film region, are due to small numerical random axial velocity disturbances on the gas–liquid interface.

The coefficients behavior is similar for the different velocities: the highest values are reached in the film zone while the tail had the lowest. It is also possible to infer the liquid velocity effect on the mass transfer coefficients: the lowest global and local coefficients are associated with the lowest liquid velocity.

Fig. 10 shows the influence of the bubble Reynolds number (based on the bubble velocity) on the average Sherwood number for the different bubble regions.

According to the data in Fig. 10, in the three regions, the average mass transfer coefficients increase with the velocity of the liquid. For each region, this data can be fitted by exponential equations defining a dependence of the Sherwood number on the bubble Reynolds number (for $M = 5.3 \times 10^{-5}$, $Sc = 1.84 \times 10^4$):

$$\overline{Sh}_{nose} = 0.26Re_B^{1.00} \quad (17)$$

$$\overline{Sh}_{film} = 4.14Re_B^{0.56} \quad (18)$$

$$\overline{Sh}_{tail} = 0.022Re_B^{1.26} \quad (19)$$

$$\overline{Sh}_{global} = 2.04Re_B^{0.66} \quad (20)$$

4.2.2.3. Mass transfer coefficients — comparison with literature. A direct comparison between the numerical values of the mass transfer coefficients with predictions given by the Eqs.

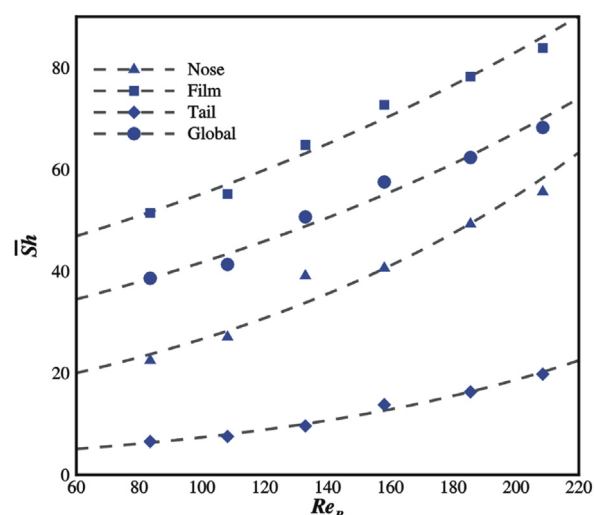


Fig. 10 – Average Sherwood number for different bubble regions in function of the bubble Reynolds number (for $M = 5.3 \times 10^{-5}$, $Sc = 1.84 \times 10^4$). The dashed lines represent the fitted equations for each zone.

(4)–(8) is not a straightforward task. In the correlations supported by the penetration theory, the coefficients are related to the superficial bubble area ($\bar{k}_L A$) and are not discriminated by hydrodynamic regions (nose, film, and tail).

Besides, these equations were developed for cases where a bubble rises through a quiescent liquid. For comparison purposes, the average Sherwood numbers acquired from Eqs. (6)–(8) and the value numerically obtained for stagnant liquid conditions are 1930, 1220, 1400 and 38.6, respectively. The theoretical and numerical values show a large difference (around two orders of magnitude), indicating that these correlations are not appropriate to describe the problem in study, at least for the dimensionless numbers considered.

The difference is very significant and, just to have an idea of its implication in terms of concentration behaviour near the interface, the concentration gradient at the interface that would lead to the referred magnitudes of \bar{k}_L is plotted in Fig. 11 (red dashed line) and compared with the profile numerically acquired (black solid line). As can be seen, the penetration theory is related to very low levels of radial diffusion: the slope of the concentration profile that justify a \bar{k}_L value in the order of 10^{-4} m s^{-1} (and Sherwood around 1400) implies a mass boundary layer with a thickness of about 0.3% of the total thickness of the liquid film, contrary to the 30% obtained by numerical simulation. A linear profile along the boundary layer, described by the film theory (where $k = \frac{D_L}{\delta_h}$) (Welly et al., 2008) is also represented by a black dashed line.

A possible justification for the high mass transfer rates obtained by researchers who have applied penetration theory may be in the experimental procedure adopted. They used a constant volume technique to determine the mass transfer coefficients: the volume of a bubble rising in a closed column filled with liquid will remain constant irrespective of the extent of gas dissolution, as long as the system is incompressible. Therefore, it was measured the rate of pressure change in the rising bubble to determine the rate of gas transfer to the liquid. However, there are always small bubbles, some visible others microscopic, which are blown out from the body of the bubble by the flow itself. These small bubbles, which do not come from the dissolution process, are taken as such in the

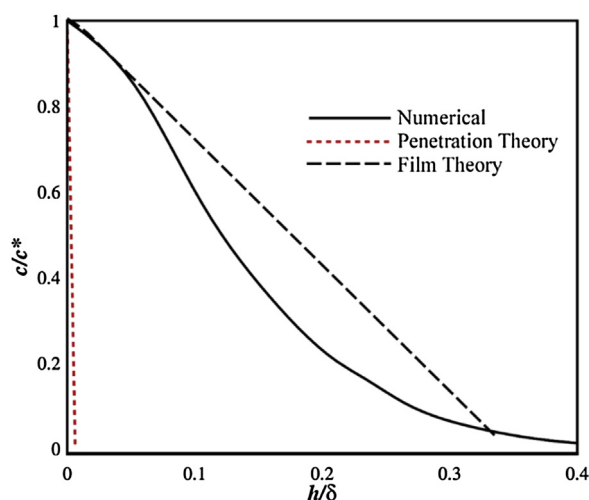


Fig. 11 – Dimensionless concentration of oxygen in the developed film region acquired by simulation (Numerical). The dotted lines represent the profiles that would produce the mass transfer coefficients values estimated by the penetration (red line) and by the film (black line) theories. The abscissas axis represents h (distance along the normal to the bubble surface) normalized by the film thickness ($M = 5.3 \times 10^{-5}$, $Sc = 1.84 \times 10^4$) (For interpretation of the references to colour in this figure legend, the reader is referred to the web version of this article).

experimental technique used. Its importance will be greater, as the rate of dissolution gets lower.

Just to have an idea, the mass transferred during the rise of a Taylor bubble through a column of stagnant liquid with 1.0 m length was calculated taking our numerical results and those given by Niranjana (Eq.(7)) for a $M = 5.3 \times 10^{-5}$ and a $Sc = 1.84 \times 10^4$. The difference between the dissolved mass estimated for these two alternatives is 1.65×10^{-9} g, which corresponds, under normal pressure and temperature conditions, to a volume of gas of 6.85×10^{-8} m³. This value is equivalent to the volume of 16 spherical bubbles of 2 mm.

4.2.2.4. Mass transfer coefficients — a simple theory for predictions. As the largest contribution to the overall mass transfer coefficient comes from the film region, a simple theory was developed that may help in future studies, namely for systems characterized by other Morton numbers.

Performing a volumetric balance in MFR between two cross sections of the column – 1) one in the undisturbed liquid above the bubble and 2) another in the developed liquid film region – it gives the following expression:

$$\pi D \delta \bar{U}_f = (U_\infty + (c - 1) \bar{U}_L) \pi \frac{D^2}{4} \quad (21)$$

and solving in order to \bar{U}_f knowing that for laminar flow $c = 2$:

$$\bar{U}_f = \frac{(U_\infty + \bar{U}_L) D}{4 \delta_H} \quad (22)$$

where \bar{U}_f is the average velocity in the developed film and δ_H the liquid film thickness. Using this value of velocity, the Re_f was solved.

Assuming a correlation in the form:

$$\bar{Sh}_{film} = a Re_f^b \quad (23)$$

and fitting to the numerical data obtained, it results:

$$\bar{Sh}_{film} = 4.05 Re_f^{0.83} \quad (24)$$

This simplified model can be very useful to provide quick estimations of gas–liquid mass transfer coefficients in slug flow systems. Nevertheless, its applicability should be validated in the future by performing similar simulations for different Morton numbers (maintaining Schmidt number). It is also important to keep in mind the large computational effort necessary to perform each simulation, i.e., around 2 months using a computer cluster with a high processing capacity.

5. Conclusions

This manuscript presents a detailed numerical study focused on the mass transfer phenomenon from Taylor bubbles of pure oxygen to co-current liquid initially absent of solute. The simultaneous solution of the flow field, bubble shape and mass transfer in a domain with stationary walls was carried out successfully. Several simulations were performed for a range of Reynolds numbers (i.e., varying the inlet liquid velocities) and fixed liquid properties (i.e., constant Morton number) with a particular interest placed on analyzing the influence of the different hydrodynamic flow regions on the bubble surroundings (nose, film and tail region).

The determination of local mass transfer coefficients for the different flow regions surrounding a Taylor bubble allows the identification of the liquid film as the largest contributor in terms of mass transfer flux. Another important aspect about the film region is the relation between the local mass transfer coefficients and the Taylor bubble length. For bubbles with a fully developed liquid film and with a length between 2–9D, these coefficients become constant and independent of the bubble length. While also contributing to the overall solute transfer to the liquid phase, the bubble tail region shows the lowest mass transfer coefficients. In terms of a global perspective of the occurring mechanism, it can be roughly concluded that the solute diffuses from the bubble nose and film surface, while the wake below the tail accumulates part of the solute transferred instead of letting it freely disperse in the liquid.

Furthermore, it was shown that if the goal is to enhance mass transfer between a Taylor bubble and liquid, an increase on the Reynolds number is able to promote an increase in the mass transfer flux in all the referred hydrodynamic regions.

Regarding the validation of mass transfer coefficient data from soluble bubbles to a flowing liquid, the Higbie penetration theory is normally used as the fundamental model for comparison (correlations of Filla (1972); Niranjana et al. (1988) and Sena Esteves and Guedes de Carvalho, (1993)). The numerical coefficients acquired during this work present a significant deviation (of two orders of magnitude) to the ones estimated from the aforementioned model. The difference between these values can be justified by the experimental procedure, that usually does not account for small bubbles that are continuously released during the bubble movement. On the other hand, the film theory seems to be more adequate to estimate the concentration gradients adjacent to the gas–liquid interface.

Globally, the results produced by this work shows the viability of using Taylor bubble to feed solute into a confined liquid system. This feature is particularly interesting in scenarios that demand a supply of reactant species to promote or enhance surface reactions. As aforementioned, the control

of biofilm formation in tube walls is a perfect example of this kind of scenarios. The use of a wider range of liquid properties to include different Morton numbers, as well as the coupling of reactive mechanisms at the wall surface, will be important features to address in future works to extend/complement the findings presented in this manuscript.

Acknowledgments

The authors acknowledge the support of FEDER funds through COMPETE2020—Operational Programme for Competitiveness Factors (POCI) and National Funds (PIDDAC) through FCT under projects PEst-OE/EME/UI0532 and POCI-01-0145-FEDER-031758. M.C.F. Silva also acknowledges the financial support provided by FCT through the PhD Grant PD/BD/ 52622/2014.

This work was also supported through computational resources provided by FEUP Cluster-Avalanche.

References

- ANSYS FLUENT Theory Guide 15317 2011; 724–746.
- Aboulhasanzadeh, B., Thomas, S., Taeibi-Rahni, M., Tryggvason, G., 2012. Multiscale computations of mass transfer from buoyant bubbles. *Chem. Eng. Sci.* 75, 456–467, <http://dx.doi.org/10.1016/j.ces.2012.04.005>.
- Aboulhasanzadeh, B., Hosoda, S., Tomiyama, A., Tryggvason, G., 2013. A validation of an embedded analytical description approach for the computations of high Schmidt number mass transfer from bubbles in liquids. *Chem. Eng. Sci.* 101, 165–174, <http://dx.doi.org/10.1016/j.ces.2013.06.020>.
- Alke, A., Bothe, D., Kroeger, M., Warnecke, H.J., 2009. VOF-based simulation of conjugate mass transfer from freely moving fluid particles. *WIT Trans. Eng. Sci.* 63, 157–168, <http://dx.doi.org/10.2495/MPF090141>.
- Aramrak, S., Flury, M., Harsh, J.B., 2011. Detachment of deposited colloids by advancing and receding air-water interfaces. *Langmuir* 27, 9985–9993, <http://dx.doi.org/10.1021/la201840q>.
- Araújo, J.D.P., Miranda, J.M., Pinto, A.M.F.R., Campos, J.B.L.M., 2012. Wide-ranging survey on the laminar flow of individual Taylor bubbles rising through stagnant Newtonian liquids. *Int. J. Multiph. Flow* 43, 131–148, <http://dx.doi.org/10.1016/j.ijmultiphaseflow.2012.03.007>.
- Bott, T.R., 1995. *Fouling of Heat Exchangers*. Elsevier Science, Amsterdam.
- Brackbill, J.U., Kothe, D.B., Zemach, C., 1992. A continuum method for modeling surface tension. *J. Comput. Phys.* 100, 335–354, [http://dx.doi.org/10.1016/0021-9991\(92\)90240-Y](http://dx.doi.org/10.1016/0021-9991(92)90240-Y).
- Campos, J.B.L.M., Guedes de Carvalho, J.R.F., 1988. An experimental study of the wake of gas slugs rising in liquids. *J. Fluid Mech.* 196, 27–37, <http://dx.doi.org/10.1017/S0022112088002599>.
- Characklis, W.G., 1981. Fouling biofilm development: a process analysis. *Biotech. Bioeng.* 23, 1923–1960, <http://dx.doi.org/10.1002/bit.260230902>.
- Cheng, K., Demirci, A., Catchmark, J.M., 2010. Advances in biofilm reactors for production of value-added products. *Appl. Microbiol. Biotechnol.* 445–456, <http://dx.doi.org/10.1007/s00253-010-2622-3>.
- Clift R., Grace J.R. and Weber M.E., *Bubbles, drops and particles*, New York: Academic Press. 1978, 97–124.
- Colón-González, M., Méndez-Ortiz, M.M.M., Membrillo-Hernández, J., 2004. Anaerobic growth does not support biofilm formation in *Escherichia coli* K-12. *Res. Microbiol.* 155, 514–521, <http://dx.doi.org/10.1016/j.resmic.2004.03.004>.
- Cui, Z., Chang, S., Fane, A.G., 2003. The use of gas bubbling to enhance membrane processes. *J. Membr. Sci.* 221, 1–35, [http://dx.doi.org/10.1016/S0376-7388\(03\)00246-1](http://dx.doi.org/10.1016/S0376-7388(03)00246-1).
- Darmana, D., Deen, N.G., Kuipers, J.A.M., 2006. Detailed 3D modeling of mass transfer processes in two-phase flows with dynamic interfaces. *Chem. Eng. Technol.* 29, 1027–1033, <http://dx.doi.org/10.1002/ceat.200600156>.
- Davidson, M.R., Rudman, M., 2002. Volume-of-fluid calculation of heat or mass transfer across deforming interfaces in two-fluid flow. *Numer. Heat Transfer B Fundam.* 41, 291–308, <http://dx.doi.org/10.1080/104077902753541023>.
- Demirci, A., Pometto 3rd., A.L., Ho, K.-L.G., 1997. Ethanol production by *Saccharomyces cerevisiae* in biofilm reactors. *J. Ind. Microbiol. Biotechnol.* 19, 299–304, <http://dx.doi.org/10.1038/sj.jim.2900464>.
- Deshpande, K.B., Zimmerman, W.B., 2006. Simulation of interfacial mass transfer by droplet dynamics using the level set method. *Chem. Eng. Sci.* 61, 6486–6498, <http://dx.doi.org/10.1016/j.ces.2006.06.012>.
- Dumitrescu, D.T., 1943. Strömung an einer Luftblase im senkrechten Rohr. *Z. Angew. Math. Mech.* 23, 139–149, <http://dx.doi.org/10.1002/zamm.19430230303>.
- Fabre, J., Line, A., 1992. Modeling of two-phase slug flow. *Annu. Rev. Fluid Mech.* 24, 21–46, <http://dx.doi.org/10.1146/annurev.fl.24.010192.000321>.
- Filla M. Ph.D Thesis, University of Cambridge, 1972.
- Flint, S.H., Bremer, P.J., Brooks, J.D., 1997. Biofilms in dairy manufacturing plant — description, current concerns and methods of control. *Biofouling* 11, 81–97, <http://dx.doi.org/10.1080/08927019709378321>.
- Floyd, K.A., Moore, J.L., Eberly, A.R., Good, J.A.D., Shaffer, C.L., Zaver, H., Almqvist, F., Skaar, E.P., Caprioli, R.M., Hadjifrangiskou, M., 2015. Adhesive fiber stratification in uropathogenic *Escherichia coli* biofilms unveils oxygen-mediated control of type 1 pili. *PLoS Pathog.* 11 (3), 1–26, <http://dx.doi.org/10.1371/journal.ppat.1004697> [art. no. e1004697].
- Fulford, G.D., 1964. The flow of liquids in thin films. *Adv. Chem. Eng.* 5, 151–236, [http://dx.doi.org/10.1016/S0065-2377\(08\)60008-3](http://dx.doi.org/10.1016/S0065-2377(08)60008-3).
- Ghosh, R., Cui, Z.F., 1999. Mass transfer in gas-sparged ultrafiltration: upward slug flow in tubular membranes. *J. Membr. Sci.* 162, 91–102, [http://dx.doi.org/10.1016/S0376-7388\(99\)00126-X](http://dx.doi.org/10.1016/S0376-7388(99)00126-X).
- González, C., Marciniak, J., Villaverde, S., León, C., García, P.A., Muñoz, R., 2008. Efficient nutrient removal from swine manure in a tubular biofilm photo-bioreactor using algae-bacteria consortia. *Water Sci. Technol.* 58, 95–102, <http://dx.doi.org/10.2166/wst.2008.655>.
- Hayashi, K., Tomiyama, A., 2011. Interface tracking simulation of mass. *J. Comput. Multiph. Flows* 3.
- Hayashi, K., Hosoda, S., Tryggvason, G., Tomiyama, A., 2014. Effects of shape oscillation on mass transfer from a Taylor bubble. *Int. J. Multiph. Flow* 58, 236–245, <http://dx.doi.org/10.1016/j.ijmultiphaseflow.2013.09.009>.
- Higbie, R., 1935. The rate of absorption of a pure gas into a still liquid during short periods of exposure. *Trans. Am. Inst. Chem. Eng.* 31, 365–389.
- Hosoda, S., Abe, S., Hosokawa, S., Tomiyama, A., 2014. Mass transfer from a bubble in a vertical pipe. *Int. J. Heat Mass Transfer* 69, 215–222, <http://dx.doi.org/10.1016/j.ijheatmasstransfer.2013.10.031>.
- Hosoda, S., Tryggvason, G., Hosokawa, S., Tomiyama, A., 2015. Dissolution of single carbon dioxide bubbles in a vertical pipe. *J. Chem. Eng. Jpn.* 48, 418–426, <http://dx.doi.org/10.1252/jcej.14we241>.
- Kreutzer, M.T., Du, P., Heiszwolf, J.J., Kapteijn, F., Moulijn, J.A., 2001. Mass transfer characteristics of three-phase monolith reactors. *Chem. Eng. Sci.* 56, 6015–6023, [http://dx.doi.org/10.1016/S0009-2509\(01\)00271-8](http://dx.doi.org/10.1016/S0009-2509(01)00271-8).
- Kumar, M., Lin, J.-G., 2010. Co-existence of anammox and denitrification for simultaneous nitrogen and carbon removal — strategies and issues. *J. Hazard. Mater.* 178, 1–9, <http://dx.doi.org/10.1016/j.jhazmat.2010.01.077>.
- Mayor, T.S., Pinto, A.M.F.R., Campos, J.B.L.M., 2007a. Hydrodynamics of gas-liquid slug flow along vertical pipes in turbulent regime. *Chem. Eng. Res. Des.* 85, 1497–1513, <http://dx.doi.org/10.1205/cherd06245>.

- Mayor, T.S., Pinto, A.M.F.R., Campos, J.B.L.M., 2007b. Hydrodynamics of gas–liquid slug flow along vertical pipes in the laminar regime-experimental and simulation study. *Ind. Eng. Chem. Res.* 46, 3794–3809, <http://dx.doi.org/10.1021/ie0609923>.
- Mayor, T.S., Pinto, A.M.F.R., Campos, J.B.L.M., 2008. Vertical slug flow in laminar regime in the liquid and turbulent regime in the bubble wake — comparison with fully turbulent and fully laminar regimes. *Chem. Eng. Sci.* 63, 3614–3631, <http://dx.doi.org/10.1016/j.ces.2008.04.020>.
- Nicklin, D., Wilkes, J., Davidson, J., 1962. Two-phase flow in vertical tubes. *Trans. Inst. Chem. Eng.* 40, 61–68.
- Niranjan, K., Hashim, M.A., Pandit, A.B., Davidson, J.F., 1988. Liquid-phase controlled mass transfer from a gas slug. *Chem. Eng. Sci.* 43, 1247–1252, [http://dx.doi.org/10.1016/0009-2509\(88\)85096-6](http://dx.doi.org/10.1016/0009-2509(88)85096-6).
- Nogueira, S., Riethmuler, M.L., Campos, J.B.L.M., Pinto, A.M.F.R., 2006a. Flow in the nose region and annular film around a Taylor bubble rising through vertical columns of stagnant and flowing Newtonian liquids. *Chem. Eng. Sci.* 61, 845–857, <http://dx.doi.org/10.1016/j.ces.2005.07.038>.
- Nogueira, S., Riethmuller, M.L., Campos, J.B.L.M., Pinto, A.M.F.R., 2006b. Flow patterns in the wake of a Taylor bubble rising through vertical columns of stagnant and flowing Newtonian liquids: an experimental study. *Chem. Eng. Sci.* 61, 7199–7212, <http://dx.doi.org/10.1016/j.ces.2006.08.002>.
- Özkan, F., Wenka, A., Hansjosten, E., Pfeifer, P., Kraushaar-Czarnetzki, B., 2016. Numerical investigation of interfacial mass transfer in two phase flows using the VOF method. *Eng. Appl. Comput. Fluid Mech.* 10, 100–110, <http://dx.doi.org/10.1080/19942060.2015.1061555>.
- Park, Y.H., Kim, E.Y., Seo, W.T., Jung, K.H., Yoo, Y.J., 1989. Production of cephalosporin C in a fluidized-bed bioreactor. *J. Ferment. Bioeng.* 67, 409–414, [http://dx.doi.org/10.1016/0922-338X\(89\)90146-3](http://dx.doi.org/10.1016/0922-338X(89)90146-3).
- Pinto, A.M.F.R., Pinheiro, M.N.C., Campos, J.B.L.M., 1998. Coalescence of two gas slugs rising in a co-current flowing liquid in vertical tubes. *Chem. Eng. Sci.* 53, 45–54, [http://dx.doi.org/10.1016/0009-2509\(95\)00254-5](http://dx.doi.org/10.1016/0009-2509(95)00254-5).
- Qureshi, F.M., Badar, U., Ahmed, N., 2001. Biosorption of copper by a bacterial biofilm on a flexible polyvinyl chloride conduit. *Appl. Environ. Microbiol.* 67, 4349–4352, <http://dx.doi.org/10.1128/AEM.67.9.4349>.
- Ratkovich, N., Horn, W., Helmus, F.P., Rosenberger, S., Naessens, W., Nopens, I., Bentzen, T.R., 2013. Activated sludge rheology: a critical review on data collection and modelling. *Water Res.* 47, 463–482, <http://dx.doi.org/10.1016/j.watres.2012.11.021>.
- Sanromán, A., Feijoo, G., Lema, J.M., 1996. Immobilization of *Aspergillus niger* and *Phanerochaete chrysosporium* on polyurethane foam. *Prog. Biotechnol.* 11, 132–135, [http://dx.doi.org/10.1016/S0921-0423\(96\)80019-0](http://dx.doi.org/10.1016/S0921-0423(96)80019-0).
- Sehar, S., Naz, I., 2016. Role of the biofilms in wastewater treatment, in: microbial biofilms — importance and applications. InTech, 121–144, <http://dx.doi.org/10.5772/63499>.
- Sena Esteves, M.T., Guedes de Carvalho, J.R.F., 1993. Liquid-side mass transfer coefficient for gas slugs rising in liquids. *Chem. Eng. Sci.* 48, 3497–3506.
- Silva, M.C.F., Araújo, J.D.P., Campos, J.B.L.M., 2017. CFD studies coupling hydrodynamics and solid–liquid mass transfer in slug flow for matter removal from tube walls. *AIChE J.* 63, 2420–2439, <http://dx.doi.org/10.1002/aic.15610>.
- Taha, T., Cui, Z.F., 2006. CFD modelling of slug flow in vertical tubes. *Chem. Eng. Sci.* 61, 676–687, <http://dx.doi.org/10.1016/j.ces.2005.07.022>.
- Taitel, Y., Barnea, D., Dukler, A.E., 1980. Modelling flow pattern transitions for steady upward gas–liquid flow in vertical tubes. *AIChE J.* 26, 345–354, <http://dx.doi.org/10.1002/aic.690260304>.
- Treybal, R.E., 1981. Mass-Transfer Operations., <http://dx.doi.org/10.1002/aic.690020430>.
- van Heuven, J.W., Beek, W.J., 1963. Gas absorption in narrow gas lifts. *Chem. Eng. Sci.* 18, 377–389, [http://dx.doi.org/10.1016/0009-2509\(63\)80030-5](http://dx.doi.org/10.1016/0009-2509(63)80030-5).
- Welty, J.R., Wicks, C.E., Wilson, R.E., Rorrer, G.L., 2008. *Fundamentals of Momentum, Heat, and Mass Transfer*.
- Yoon, S.S., Hennigan, R.F., Hilliard, G.M., Ochsner, U.A., Parvatiyar, K., Kamani, M.C., Allen, H.L., Dekievit, T.R., Gardner, P.R., Schwab, U., Rowe, J.J., Iglewski, B.H., Mcdermott, T.R., Mason, R.P., Wozniak, D.J., Hancock, R.E.W., Parsek, M.R., Noah, T.L., Boucher, R.C., Hassett, D.J., 2002. *Pseudomonas aeruginosa* anaerobic respiration in biofilms: relationships to cystic fibrosis pathogenesis. *Dev. Cell* 3, 593–603.
- Youngs, D., 1982. Time-dependent multi-material flow with large fluid distortion. *Numer. Methods Fluid Dyn.*, 273–285.